Positron Emission Tomography of Not-Full-Ring Sensors Arrangement: Simulation and Verification for Internal Imaging of Hydraulic Cylinder

CHEN HAO [1], **MIN ZHAO** [1], **MIN YAO** [1], **RUIPENG GUO** [1],
MINGWEI ZHU [1], **AND XIAO HUI** [2]

[1]College of Automation Engineering, Nanjing University of Aeronautics and Astronautics, Nanjing 211106, China
[2]College of Artificial Intelligence, Nanjing University of Aeronautics and Astronautics, Nanjing 211106, China

Corresponding author: Chen Hao (chenhaonuaa@163.com)

ABSTRACT The research goal of this article is to imaging the oil distribution in landing gear hydraulic cylinder by Positron Emission Tomography(PET). Considering the flexibility and commercial cost for automation testing, two kinds of Not-Full-Ring sensors arrangement, Uniform-arrangement and Bilateral-arrangement, are proposed. The Full-Ring PET is used as the contrast template of imaging. Firstly, GATE 7.1 is used as the Monte Carlo simulation platform to simulate the sensors arrangement of the two Not-Full-Ring schemes. The results of scattering fraction, sensitivity and photon energy distribution were used to evaluate the feasibility of the two schemes. Then, a set of verification device with rotating platform and variable sensing diameter is constructed. The two kinds of Not-Full-Ring sensors arrangements were verified through the verification device. By imaging the hydraulic oil in the hydraulic cylinder, the results were evaluated and compared by using Signal Noise Ratio(SNR). According to the simulation and verification results, Not-Full-Ring scheme is feasible for imaging the liquid distribution in the hydraulic cavity. Uniform-arrangement has a more better imaging performance than Bilateral-arrangement. Such sensors arrangement scheme is not only suitable for this research, but also suitable for other PET imaging applications which need to consider the flexibility and commercial cost.

INDEX TERMS Positron emission tomography, gamma photon sensor, PET sensing and imaging, PET sensors arrangement.

I. INTRODUCTION

Aircraft landing gear is one of the key components of aircraft, which needs to meet the requirements of aircraft in high load takeoff and landing conditions. Landing gear structure is a set of hydraulic system, and its core actuator are hydraulic cylinders and hydraulic dampers. The essence of landing gear performance test is to test the hydraulic system health, including drop test, shimmy test and sudden extension test. The health monitoring of landing gear is one of the research

The associate editor coordinating the review of this manuscript and approving it for publication was Zhanyu Ma .

hotspots of aircraft safety. At present, the main research focuses on comprehensive performance test and dynamic simulation. Orlando, C studied the wear problem of aircraft nose landing gear, optimized the shimmy suppression ability of hydraulic cylinder, and carried out simulation and verification [1]. Rahmani, M *et al.* studied the shimmy damper of landing gear and designed a new structure of shimmy damper for nose landing gear [2]. Cristiani, D, *et al.* simulated the load variation of aircraft landing process. The landing gear was used as the connection between dynamic domain and structural domain, and the displacement and force of landing gear position were analyzed [3]. Merino Martinez, R *et al.*

Measured and simulated the noise emission and stability of full-scale nose landing gear in wind tunnel [4]. Pytka, J *et al.* measured the force and torque acting on the landing gear by strain force sensor [5].

At present, there are few researches about the testing of landing gear hydraulic circuit. In this article, a kind of sensors arrangement scheme, based on Positron Emission Tomography(PET), is studied and proposed, which is suitable for the general industrial nondestructive imaging. This imaging scheme is not only for the oil circuit of the landing gear hydraulic cylinder, but the other types of tubes and cavities. By sensing the oil distribution with medical level radiation, the hydraulic performance can be imaging, and then the wear condition can be analyzed according to the results of reconstructed image.

At present, mature commercial PET device is mainly used in the biomedical field for human and small animals. The traditional PET structure is composed of sufficient sensors spliced into a ring. Due to the high unit-price of the sensor and fixed sensing diameter of the ring, it can not meet the demand of the industrial field which pays attention to the commercial cost performance and the automation flexibility. In this context, this article will simulate and verify the feasibility of Not-Full-Ring structure, that is, PET with fewer sensors and variable sensing diameter. **Figure 1(a).** shows the traditional Full-Ring structure and our application prospects in Not-Full-Ring structure.

In recent years, more and more research teams are developing special PET devices in various fields to meet their research needs. Our designs refer to these cases. Yang *et al.* studied the characteristics of fluid in industrial parts through PET with flat plate sensors. However, in order to improve the tracking speed, the experiment realized positioning by counting gamma photon pairs instead of imaging [6]. David J *et al.* proposed the idea of using PET to observe the distribution of lubricating oil in aero-engine [7]. Streun M *et al.* used PET to study the metabolism and physiological function of plants. The detectors of their system are arranged in a horizontal plane to allow the plants to be measured in the natural upright position. Two groups of four detector modules stand face-to-face and rotate around the field-of-view. This special system geometry requires dedicated image reconstruction and normalization procedures [8]. Wang *et al.* developed a plant specific high-resolution PET imaging detection device, the system adopts a ring structure, which can detect the vertical growing plants in the circumferential and vertical directions, and the number of sensors is reduced, and the detection cost is greatly reduced [9]. Tasima *et al.* proposed an open double ring PET, which can bring patients more comfortable space. On this basis, the double ring model is optimized to an elliptical single ring model, and the elliptical one can maintain the original system sensitivity and reduce the cost [10]. Raylman *et al.* developed a small high-resolution PET named ''tandempet''. By arranging crystal sensors with different resolutions on both sides, the optimal position of detector resolution can be adjusted [11]. Corrector *et al.* evaluated the
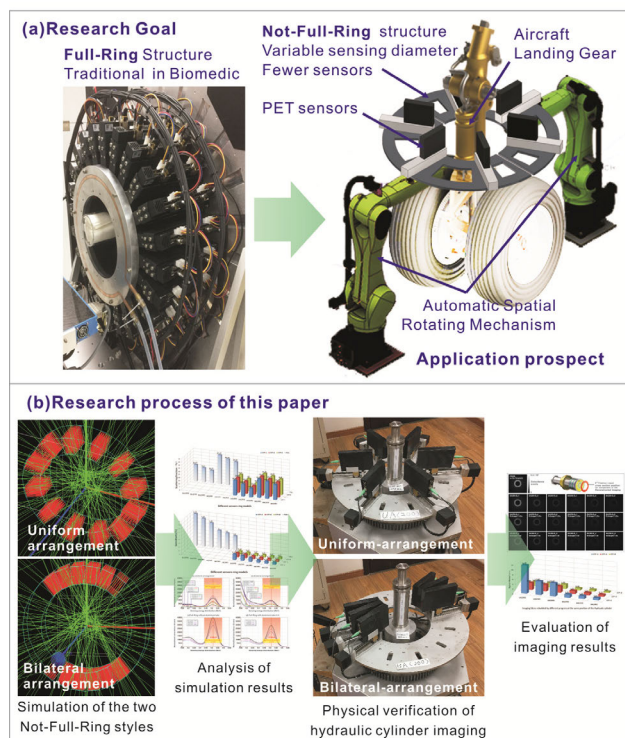
FIGURE 1. The research ultimate goal and studying process of this article. (a) Research goal, design a PET system with fewer sensors and variable sensing diameter. (b) Research process of this article, simulation and analysis the results, verification the system and evaluation the imaging results.

performance of a single PET sensor in the geometric distance. They developed a new PET with 8 detectors based on SiPM and monolithic LYSO crystals. This design can accurately determine the centroid of the scintillation light distribution [12]. Y. Chen, K. Saha *et al.* designed a full ring breast PET scanner consisting of 96 rings. They used **GATE** to simulate the system and used SNR to evaluation of imaging quality [13]. Kobayashi, T *et al.* developed a multi-modal compatible flexible PET scanner. the scanner consists of adjustable two detector units and their support apparatus, and then scans a patient lying on a bed equipped by other medical imaging/non-imaging device. Therefore, depending on the size and shape of the patient and the patient bed and other demands, the detector geometry can be changed flexibly [14]. Chih-Chieh Liu *et al.* proposed a crystal arrays with curved surfaces to reduce the dead space between detector modules and hence improve the sensitivity of PET. They used detectors based on SiPM arrays coupled to both ends of scintillator arrays with finely segmented and long detector elements [15]. Before this study, we have done some preliminary research work, including imaging of positron tracer distribution in metal cavity and scattering correct algorithm [16], [17].

In this article, as shown in **Figure 1(b).**, we will simulate and verify the performance of the two Not-Full-Ring sensors arrangement styles. The Not-Full-Ring structure includes 3 pairs of sensors. The sensors can rotate around the center of
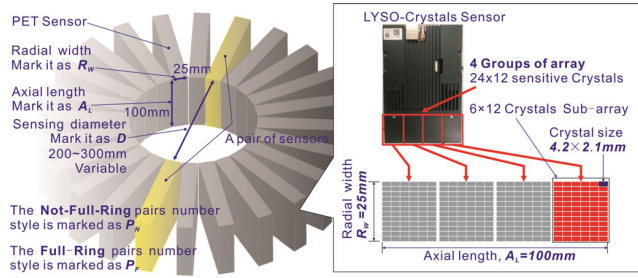
FIGURE 2. Modeling parameters of sensors-Ring arrangement. In the Full-Ring arrangement, the arrangement scheme and space size of sensors, the sensitive crystals arrangement structure of a single sensor.

TABLE 1. Sensor parameters.

PARAMETER	VALUE
Axial Length	100mm
Radial width	25mm
Sensitive material	LYSO
Single crystal size	4.2×2.1×20mm3
Scintillator array	24×12
Photoelectric converter	24x12 silicon photomultiplier(SiPM) array
Energy resolution	15%
Energy reference value	511keV
Time resolution	310ps
Coincidence time window	2ns
Energy window	250~650keV
Dead time	300ns

the sensing ring, and can also move along the radial direction of the sensing ring. This article will describe the research process and results in detail from modeling and simulation of Not-Full-Ring sensors arrangement styles, comparison of simulation results of the two styles in system performance and verification of Not-Full-Ring sensors arrangement styles.

II. MODELING AND SIMULATION OF NOT-FULL-RING SENSORS ARRANGEMENT STYLES

This article used **GATE 7.1** for modeling and simulation. In this section, two styles of sensors arrangement will be constructed. The simulation data are output as coincidence events in **ROOT** format. We will evaluate the system performance of the two arrangement types by the coincidence events parameters, including scattering fraction, sensitivity and energy distribution.

A. MODELING OF SENSORS ARRANGEMENT

The actual Not-Full-Ring PET sensing system will be arranged by 3 pairs of sensors. The sensor model is **TRANS-PET BDMII** manufactured by **RAYCAN Technology Co., Ltd. (Suzhou)**. The sensor parameters are shown in **Table 1.** and **Figure 2.**. The simulation will be modeled according to the actual device parameters.

As shown in **Figure 2.**, 24 × 12 sensitive crystals divided into four groups, each group contains one 6 × 12 crystals sub-array. R_W is the linear width occupied by the sensor on the circumference of the ring, which is 25mm. A_L represents the axial depth of the sensing area. According to the design requirements, the sensing area should be adjustable in the range of diameter (marked as D) 200~300mm. The relationship between the Full-Ring pairs number of sensors and the sensing area diameter is shown in **Eq.(1)**.

$$P_F = \pi D \big/ 2R_W \tag{1}$$

As shown in **Eq.(1)**, P_F represents the Full-Ring pairs number of sensors, D represents the sensing diameter. In this article, Not-Full-Ring style that used 3 pairs of sensors are modeled according to D = 200mm, 250mm and 300mm. The Full-Ring model is used as reference. The models of Uniform-arrangement and Bilateral-arrangement constructed in **GATE 7.1** are shown in **Figure 3.**


FIGURE 3. The models constructed in GATE 7.1. The 9 simulation models, sensing diameter from 200mm to 300mm, the arrangement styles include Uniform-arrangement, Bilateral-arrangement and Full-Ring.

B. MODELING OF RADIOACTIVE SOURCE

Physical effects are added after the sensors' arrangement models complete, that including positron annihilation, photoelectric effect, Compton scattering and Rayleigh scattering.

The sensing system is designed for the imaging in industrial field, which mainly detects the low density liquid distribution in the metal cavity. The ratios of γ photons' scattering and attenuation are larger than that of biological material. In order to make the model consistent with the actual verification, aluminium material parameters are added to the **GATE 7.1** material database.

As shown in **Figure 4(A).**, the radiation source model is designed in the aluminium tube. Due to the large number of models to be simulated, it is necessary to reduce the
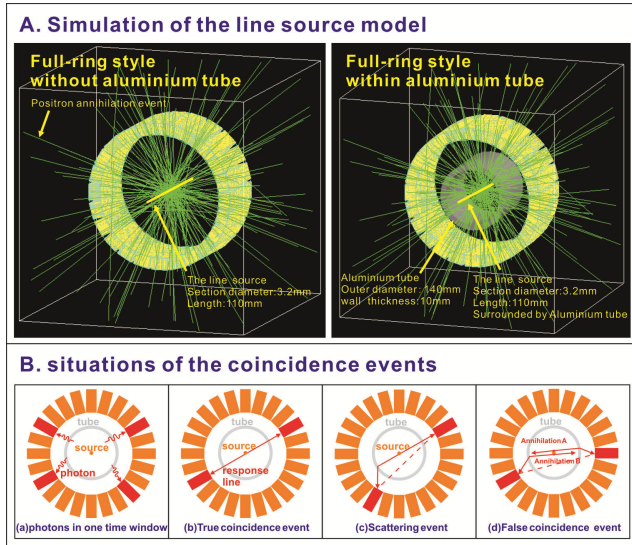
FIGURE 4. A. The location relationship of Line source model and the aluminium tube. The line source not covered by aluminum tube is regarded as routine biological test. The line source covered by aluminum tube is the condition of all Not-Full-Ring model simulations in this article. B. The four situations of the coincidence events.(a) Multiphotons in one time window, (b) True coincidence event, (c) Scattering event, (d) False coincidence event.

FIGURE 5. Simulation strategy of rotation process. The essence of rotation sensing is to discretize the continuous motion.

simulation time in order to improve the efficiency. We made some compromises on the premise that the experimental samples are reliable. Since the core purpose of this article is to verify the system performance of the Not-Full-Ring models, the most important objective of the simulation is to obtain the parameters related to the system performance. Therefore, in the simulation, the radiation source is set as Line source with uniform distribution. The axial length of the line source is 110mm, the diameter is 3.2mm, and the total activity is 10MBq, which means $10^7 \gamma$ photon pairs are emitted per second. The outer diameter of the aluminum tube is 140mm, the wall thickness is 10mm. The aluminium tube and line source are overlapped with the axis of sensors-ring. For comparison, the line source models without aluminium tube in sensors-ring will also be simulated.

After the line source was set, we defined the data acquisition rules of the sensors ring. In **GATE 7.1**, the sensors ring first records the position, energy and number of photons flying into the same time window. Then, the coincidence events are filtered according to these parameters of photons. As shown in **Figure 4(B).**, there are four situations: (a) multi-photons in one time window, (b) true coincidence events, (c) scattering events, (d) false coincidence events.

For situation (a), in **GATE 7.1** simulation, this event is directly abandoned (commercial PET also adopts this coping strategy). For situation (b, c, d), it is necessary to set the photon energy threshold manually to further screen. The true coincidence event means that the energy of the two photons are in the 511KeV range. The scattering event means that one of the two photons has an energy lower than 511KeV range.
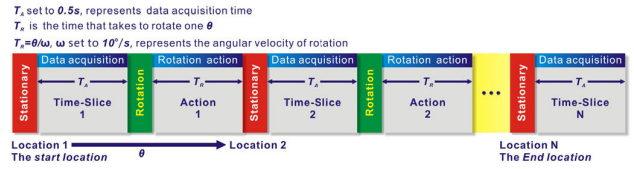
The false coincidence event means that the energy of both photons is lower than 511keV range.

The definition of 511keV range depends on the simulation results of photon energy distribution and the detection performance of the actual sensor. In **Sec III.**, we will first analyze the photon energy distribution, then define the coincidence event according to the photon energy distribution, and finally evaluate the scattering fraction and system sensitivity according to the proportion of coincidence events.

C. MODELING OF ROTATION SENSING STRATEGY

The essence of rotation sensing is to discretize the continuous motion. As shown in **Figure 5.**, each Time-Slice of the sensors-ring's rotation is regarded as a static measurement, in which the source model data is collected. T_A represents data acquisition time and is set to 0.5s, which means each Time-Slice is a interval of period 0.5s. The simulation of rotation process is realized by rotating the geometric model of the sensors-ring between two Time-slices. T_R represents the time cost by each rotation action. We mark the step angle of each rotation movement as θ. We set a constant angular velocity $\omega = 10°/s$ and $T_R = \theta/\omega$.

The relevant parameters of rotation are calculated as follows. According to **Table 1.** and **Figure 2.**, single crystal size is 4.2mm×2.1mm, the linear width occupied by crystal on the circumference of the ring is 2.1mm, we marked it as C_W, and $R_W = 12 \times C_W$. The center angle of C_W on the ring is marked as σ. The step angle θ should be an integral multiple of σ. We mark the value of integral multiple as S_{TP}, and $\theta = \sigma \times S_{TP}$. In the Not-Full-Ring style, we mark the number of sensor pairs as P_N. The number of rotation times required by the system to finish a full ring is marked as N. The geometric model of rotation parameters is shown in **Figure 6.**

As shown in **Figure 6.**, according to **Eq.(1)** and Arc Length Formula, **Eq.(2)** can be deduced as follow:

$$\sigma = \frac{\pi}{12 \cdot P_F} \tag{2}$$

For Uniform-arrangement, the number of rotation times to cover a full ring is N_U. According to **Figure 6.** and **Eq.(1,2)**, the calculation formula of N_U is shown in **Eq.(3)**

$$N_U = \frac{\pi - \sigma \cdot P_N \cdot 12}{P_N \cdot \theta} + 1 \tag{3}$$

For Bilateral-arrangement, the number of rotation times to cover a full ring is N_B. According to **Figure 6.** and **Eq.(1,2)**,
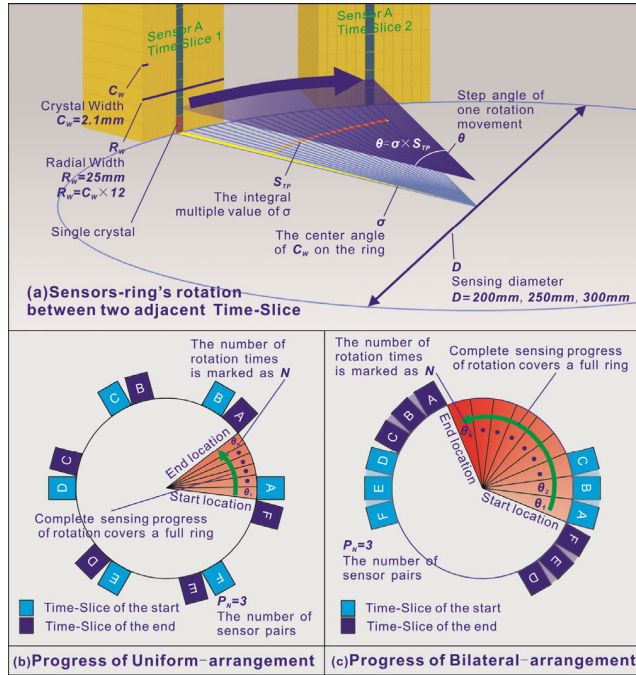
FIGURE 6. Geometric model of rotation parameters. (a)The geometric model of a single crystal in a sensor. (b)The progress of Uniform-arrangement. (c)The progress of Bilateral-arrangement.

the calculation formula of N_B is shown in **Eq.(4)**

$$N_B = \frac{\pi - \sigma \cdot P_N \cdot 12}{\theta} + 1 \tag{4}$$

When the the number of rotation times to cover a full ring has been confirmed and according to **Figure 5.**, the calculation formula of the time to complete a complete acquisition is shown as **Eq.(5)**. T_F represents the time of a complete acquisition. N represents N_U in Uniform-arrangement and N_B in Bilateral-arrangement.

$$T_F = N \cdot (T_A + T_R) - T_R \tag{5}$$

According to **Figure 6.** and **Eq.(3,4,5)**, the rotation parameters for **GATE 7.1** simulation are grouped in **Table 2.**, T_{FU} represents the total sampling time in Uniform-arrangement, and T_{FB} represents the total sampling time in Bilateral-arrangement.

As shown in **Table 2.**, we set up a list of 24 models to be simulate. The model name "UA(200)-1" means Uniform-arrangement, $D = 200$mm, $S_{TP} = 1$. By the same naming rules, "BA(300)-4" means Bilateral-arrangement, $D = 300$mm, $S_{TP} = 4$. "FR(200)" means Full-Ring style with aluminium tube in it, $D = 200$mm. "Bio(250)" means Full-Ring style without aluminium tube, $D = 250$mm.

III. COMPARISON OF SIMULATION RESULTS OF THE TWO STYLES IN SYSTEM PERFORMANCE

After all the 24 models in **Table 2.** have been simulated, we evaluated coincidence events data of each model. In this section, The evaluate results will be analyzed in detail

TABLE 2. The list of all the 24 models simulation configuration.

|								
		P_N=3, T_A=0.5s, ω=10°/s						
No.	Model Name	D(mm)	σ(°)	S_{TP}	θ(°)	N_U	T_{FU}(s)	N_B	T_{FB}(s)
1,	UA(200)-1,			1	1.25	37	23	109	68
2	BA(200)-1	200	1.25						
3,	UA(200)-4,			4	5	10	9.5	28	27.5
4	BA(200)-4								
5,	UA(200)-8,			8	10	5	7	14	20
6	BA(200)-8								
7,	UA(250)-1,			1	1	49	29.3	145	86.9
8	BA(250)-1	250	1						
9,	UA(250)-4,			4	4	13	11.3	37	32.9
10	BA(250)-4								
11,	UA(250)-8,			8	8	7	8.3	19	23.9
12	BA(250)-8								
13,	UA(300)-1,			1	0.83	61	35.5	181	105.5
14	BA(300)-1	300	0.83						
15,	UA(300)-4,			4	3.32	16	13	46	38
16	BA(300)-4								
17,	UA(300)-8,			8	6.64	8	9	23	26.5
18	BA(300)-8								
19	Bio(200),	200	In all the Full-Ring models, the acquisition time is set to 100 s						
20	FR(200)								
21,	Bio(250),	250							
22	FR(250)								
23,	Bio(300),	300							
24	FR(300)								

from energy distribution, scattering fraction and sensitivity. Through these three aspects, the system performances of the two arrangement styles are evaluated comprehensively. And the two styles will be verified by real sensors system in the next chapter.

A. PHOTON ENERGY DISTRIBUTION
When positron annihilation 511KeV γ photons penetrate through the aluminum tube wall from the radioactive source, Compton scattering is likely to occur, resulting in energy loss and ray angle deflection. Since Compton scattering probability is proportional to atomic number, and industrial parts are generally metal materials, the photon energy distribution is able to reflect the scattering distribution of industrial field.

As shown in **Figure 7(A).**, Photon energy distribution statistics presented the energy distribution of all photons detected by the sensors. According to it, we can evaluate whether the sensor can adapt to industrial sensing and imaging. The sensor filters the scattering events by setting the energy window. If the energy window is too small, a large number of real coincidence events will be excluded. If the energy window is too large, a large number of scattering events will be included. Therefore, The photon energy distribution can provide a very effective reference for the threshold setting of energy window.

The range of the sensor's energy window used in this article is 250KeV~650KeV (**Table 1.**). For industrial field, we take
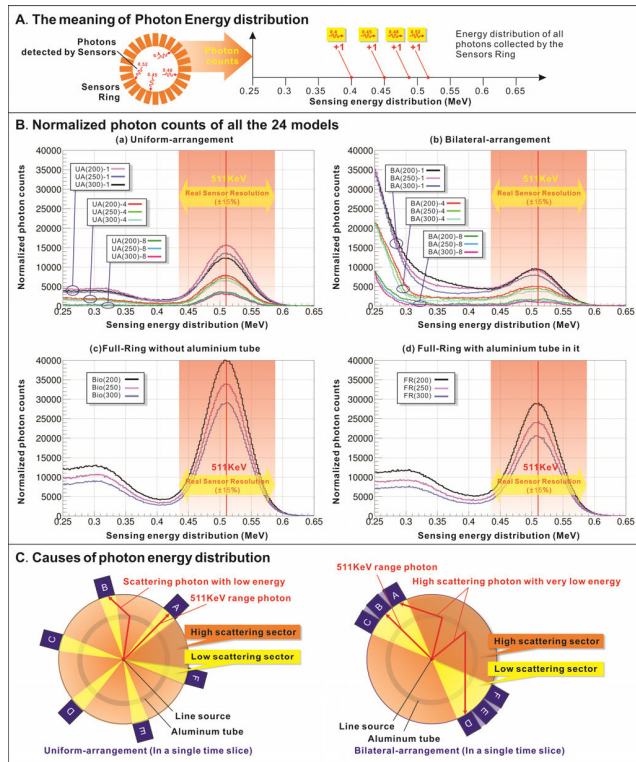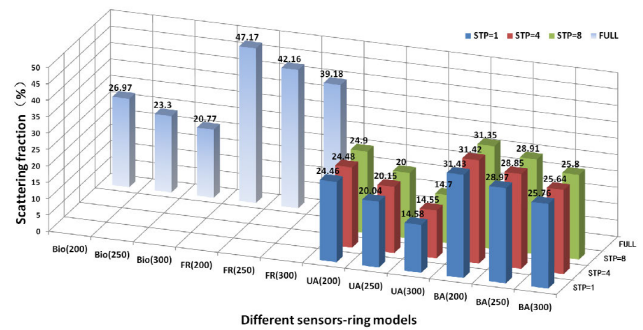
FIGURE 7. The photon energy distribution. A. The meaning of photon energy distribution. B. Photon energy distribution data of all models, among them, (a)The energy distribution detected by the 9 Uniform-arrangement models. (b)The energy distribution detected by the 9 Bilateral-arrangement models. (c)The energy distribution detected by the 3 Bio models.(d)The energy distribution detected by the 3 Full-Ring models. C. Causes of photon energy distribution, Bilateral-arrangement has two larger high scattering sector than Uniform-arrangement.

FIGURE 8. The scattering fraction of the 24 models.
UA,Uniform-arrangement. BA, Bilateral-arrangement. FR, Full-Ring style with aluminium tube in it. Bio, Full-Ring style without aluminium tube.
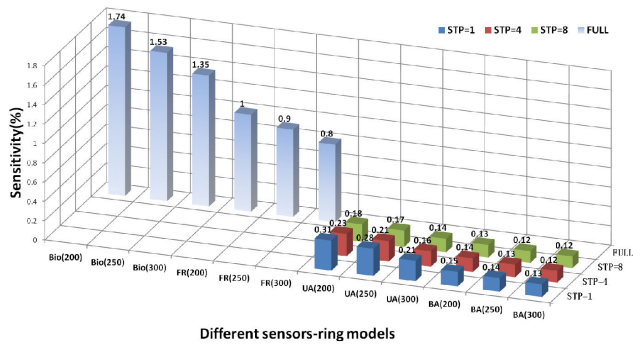
events. At the same time, Bilateral-arrangement had a large number of false coincidence events, and its effective utilization of photon pairs is obviously lower than that in Uniform-arrangement.

As shown in **Figure 7(C).**, in a single Time Slice, the sensors of Bilateral-arrangement models are concentrated, forming two large high scattering sectors. Therefore, the sensors will collect a large number of scattering photons from the two high scattering sectors. The larger the scattering angle, the lower the photon energy. That is the reason for Bilateral-arrangement having significantly large scattering in low energy(250~300 KeV). In contrast, the sensors of Uniform-arrangement models are evenly distributed on the circumference, and the angle of scattering sectors are small and dispersed, so it is not easy to receive higher scattering photons.

Although the simulation in this article used a line source model, it is easy to infer that Bilateral-arrangement models would collect a large number of high scattering photons in other ray sources as well.

B. SCATTERING FRACTION

Compared with biological field, in the industrial field, γ photons need to penetrate high-density materials, so Compton Scattering is more likely to occur. Therefore, it is necessary to pay attention to the influence of such scattering on evaluate system performance. The scattering we define in **GATE 7.1** simulation is that the photons from the line source penetrate the metal and deflect. Scattering fraction is usually used to measure the sensitivity of the sensor to scattering events, that is, the proportion of scattering coincidence events to total coincidence events. Large scattering fraction means a high rate of false-events in coincidence events sensed by the system, which will lead to imaging distortion. In **GATE 7.1**, we distinguished the scattering event from the false coincidence event according to the energy of the photon pair. Scattering events in our simulation refer to one photon in the 511KeV range and the other below the 511KeV range. **Figure 8.** shows the scattering fraction obtained from simulation data for all the 24 models.

the upper and lower 15% of 511KeV (According to the Energy resolution in **Table 1.**) as the actual energy window boundary, 430KeV~590KeV. The corresponding results of the energy window and photon energy distribution are shown in **Figure 7(B).**

As shown in **Figure 7(B).**, for all models, the energy window covers the valley and peak values on both sides of 511KeV. The sensing diameter D does not affect the distribution of photon energy, but only the total number of the photon counts. The step angle has a great influence on the number of photon counts. The smaller the step angle (represented in integral multiple S_{TP} 1, 4, 8) is, the larger the total counts is.

In the Uniform-arrangement models, the number of photons in the energy window range is more than that of scattering photons. In the Bilateral-arrangement models, the number of photons in the energy window range is significantly less than that in the Uniform-arrangement ones. It can be easily inferred that there are a lot of scattering events and false coincidence events in the large angle scattering region (250KeV ~ 330KeV).

The photon energy distribution confirms the applicability of the real sensor and reflects that the Uniform-arrangement is better than the Bilateral-arrangement in filtering scattering

FIGURE 9. The sensitivity values of all the 24 models. UA, Uniform-arrangement. BA, Bilateral-arrangement. FR, Full-Ring style with aluminium tube in it. Bio, Full-Ring style without aluminium tube.

As shown in **Figure 8.**, for the Full-Ring situation, the existence of aluminum tube leads to a significant increase of scattering events collected by the system. The scattering fraction of Not-Full-Ring style is lower than which of the Full-Ring style. S_{TP} has little effect on scattering fraction. When sensing diameter D increases, the scattering fraction decreases.

It can be concluded from **Figure 8.**, the scattering fraction of the 9 Uniform-arrangement models are lower than that of the Bilateral-arrangement ones, which are the lowest among all the 24 models.

C. SENSITIVITY

The sensitivity represents the ratio of the coincidence events number sensed by the system to the actual annihilation events per unit time. It reflects the efficiency of system sensing coincidence events. The sensitivity is mainly determined by the number and arrangement of sensors. The sensitivity values of all the 24 models are shown in **Figure 9.**.

As shown in **Figure 9.**, The sensitivity of all the Not-Full-Ring style is significantly lower than the Full-Ring style. Which means that both Uniform-arrangement and Bilateral-arrangement systems are far less sensitive than Full-Ring systems. Not-Full-Ring style systems need to spend more data acquisition time for more coincidence events to rebuild high quality imaging.

However, the sensitivity weakness of all the Not-Full-Ring style is expected. Compared with the Full-Ring system, on the premise of the sensing requirements, making appropriate compromise in sensitivity to reduce the system cost to 16% (18pairs) ∼ 25% (12pairs) is worth commercial.

IV. VERIFICATION OF NOT-FULL-RING SENSORS ARRANGEMENT STYLES

Through all the sensors-ring models simulation, we find that although the sensitivity of Not-Full-Ring is much lower than that of Full-Ring, there is no obvious disadvantage in scattering distribution and photon energy distribution. For the two Not-Full-Ring styles, Uniform-arrangement is superior
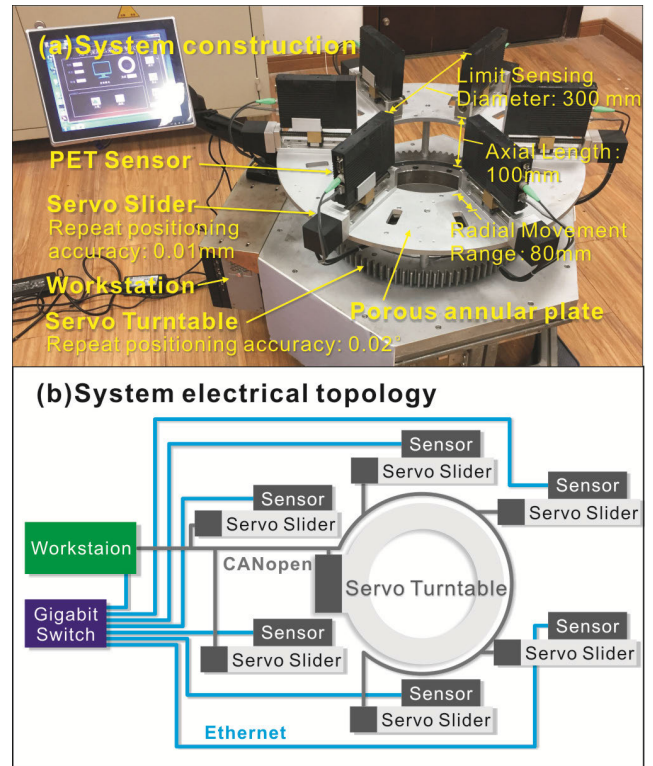

FIGURE 10. System construction and electrical topology. (a) the main motion parts of the system include 1 Servo turntable and 6 Servo sliders. (b) The Servo turntable and Servo slider are connected to the Workstation through CANopen bus. And the 3 pairs of sensors are connected to the Workstation through Gigabit switch.

to Bilateral-arrangement in scattering distribution, sensitivity and photon energy distribution.

In this section, we will verify the above simulation results by sensors-ring hardware construction, internal sensing process of the hydraulic cylinder and Signal-Noise Ratio(SNR) of reconstructed imaging.

A. HARDWARE CONSTRUCTION

The sensing space size of the hardware system is consistent with the simulation models mentioned above. As shown in **Figure 10(a).**, the main motion parts of the system include 1 Servo turntable and 6 Servo sliders. The Servo turntable is a high-precision worm wheel turntable, which is controlled by an absolute servo motor. Its rotation repeat positioning accuracy is 0.02° and meets the accuracy requirements of the single crystal center angle σ (0.83° ∼ 1.25°). In order to realize the two sensors arrangements mentioned above, a porous annular plate is installed on the rotating body of the Servo turntable. The 6 Servo sliders can be fixed on the porous annular plate according to the arrangement of sensors in the simulation models. The linear repeat positioning accuracy of the Servo slider is 0.01mm, which meets the accuracy requirement of sensing diameter D (0.1mm). The effective moving distance of each Servo slider is 80mm, which meets the range of sensing diameter D, 200mm∼300mm(limit only
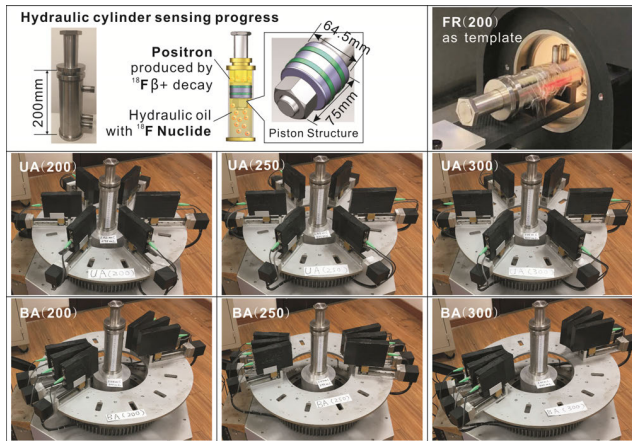
FIGURE 11. Hydraulic cylinder sensing process. For example, "FR(200)" means Full-Ring, D = 200mm, the standard template. "UA(200)" means Uniform-arrangement, D = 200mm. "BA(300)" means Bilateral-arrangement, D = 300mm.

50mm for each Servo slider). The Servo turntable and Servo slider are connected to the Workstation through **CANopen** bus.

The sensors are installed on the Servo sliders' slide blocks. The sensor TRANS-PET BDM II is a digital γ photon detector based on high-speed Silicon Photo-multiplier(SIPM) with LYSO crystals, the sensing position can be flexibly adjusted according to the detection requirements, and the ultra-high time resolution performance required for imaging can be provided. As shown in System Electrical Topology of **Figure 10(b).**, 3 pairs of sensors are connected to the Workstation through Gigabit switch. The Workstation reads the coincidence events data of the sensor system through Gigabit Ethernet network.

The software system of the Workstation controls the motion of Servo turntable and Servo sliders, and records the rotation angle and displacement in real time. At the same time, according to the acquisition strategy mentioned above, the software system collects the coincidence events data of the sensor system when the Servo turntable stops. It should be noted that, since the real-time angle information of the response line obtained by the sensor is relative angle, it is necessary to be converted into absolute angle information according to the rotation angle of Servo turntable. The coincidence events data are recorded in the list mode, including angle and energy information of each response line. When the sensing process accomplish, the response lines data list will be used to reconstruct the imaging.

B. INTERNAL SENSING PROCESS OF THE HYDRAULIC CYLINDER

In order to verify the feasibility of our application assumption and the simulation models mentioned above, the experimental process is shown in **Figure 11.,** First, in order to adapt to the range of sensing diameter D, we customized a reduced scale hydraulic cylinder of the aircraft landing gear. This hydraulic

cylinder is made of aluminum. Its outer cylinder has a wall thickness of 5mm, an inner diameter of 65mm and a length of 200mm. The piston diameter is 64.5mm, the length is 75mm, and the effective stroke is 100 mm. It is fixed on the actuating rod by an M24 nut. The piston and the inner wall of the outer cylinder are sealed by two O-rings. Our sensing imaging area is set at the piston position, and the target is the nut on the lower part of the piston. Because of its obvious cross-section shape characteristics, it is easy to compare and analyze the reconstructed images.

In order to be close to the real application scene, we use water-soluble hydraulic oil as the solvent of radiation source. Water-soluble hydraulic oil is widely used in aviation hydraulic system because of its high temperature resistance. For this experiment, due to the water solubility of the hydraulic oil, the commonly used medical positron nuclides(^{18}F-fluorodeoxyglucose) can be easily and evenly dissolved in the hydraulic oil. With the help of the experts in **RAYCAN Technology Co., Ltd. (Suzhou)**, we successfully prepared the required aviation hydraulic oil containing ^{18}F and injected it into the hydraulic cylinder.

Due to the limitation of practical conditions, we do not have Full-Ring reference system of sensing diameter D at 250mm and 300mm. Therefore, we use the commercial PET device, model **TRANS-PET-180**, as the standard reference imaging template for all arrangement styles. **TRANS-PET-180** has 12 pairs of TRANS-PET BDM II sensors with a sensing diameter of 200 mm, and its actual diameter for placing object is 180 mm. Its coincidence events data records format and imaging reconstruction algorithm are completely consistent with our Not-Full-Ring system. We will adjust the imaging reconstructed at sensing diameter 250 mm and 300 mm to that at 200 mm for quantitative comparison of imaging quality.

As shown in **Figure 11.**, "FR(200)" means Full-Ring, $D =$ 200mm, the standard template. "UA(200)" means Uniform-arrangement, $D = 200$mm. "BA(300)" means Bilateral-arrangement, $D = 300$mm. According to the 9 arrangements to be verified in **Figure 11.**, we subdivide the experimental process into 19 in **Table 3.**

As shown in **Table 3.**, considering the half-life of ^{18}F (110 minutes) and the actual application scenes, it is appropriate to set the processing Time at 600s (10min) for each experiment. In the field of industrial non-destructive imaging, the 10min sensing period is normal in commercial. During this period, the radioactivity of positron nuclide is relatively stable. For Not-Full-Ring system, stable radioactivity can ensure the imaging quality. According to the process Time, and refer to T_F and S_{TP} in **Table 2.**, In the same Time length(600s), the times of complete acquisition (Times of T_F, **Table 3.**) is different under the various step angle integral multiple S_{TP}. For example, About 600s, process "UA200 STP-1" can complete 25 trips of a full ring in 604s. As comparison, process "UA200 STP-4" has a larger S_{TP}, so it can complete 62 trips of a full ring in 604s. In each

TABLE 3. The list of subdivide experimental processes.

No.	Process ID	S_{TP}	Times of T_F	Time(s)	Radioactivity (mCi)	Liquid injection volume (ml)
1	FR200			600	1.06	308
2		1	25	604	1.02	298
3	UA200	4	62	604	1.05	298
4		8	82	603	1.09	298
5		1	18	592	1.05	301
6	UA250	4	49	609	1.07	301
7		8	70	602	1.07	301
8		1	15	593	1.01	300
9	UA300	4	44	601	1.04	300
10		8	61	601	1.09	300
11		1	8	589	1.04	300
12	BA200	4	21	606	1.06	300
13		8	27	594	1.09	300
14		1	6	560	1.03	299
15	BA250	4	17	589	1.01	299
16		8	24	608	1.07	299
17		1	5	583	1.01	300
18	BA300	4	14	574	1.02	300
19		8	21	588	1.05	300

experiment, we stabilized the radioactivity at 1mC and the injection volume at 300ml.

C. SIGNAL-NOISE RATIO OF RECONSTRUCTED IMAGING

After completing the above tests, we get the response lines data list of the 19 processes. In order to evaluate the imaging quality objectively and fairly, all experimental data are reconstructed by the same algorithm procedure. In this article, although the reconstruction algorithm process is not the innovation and research point, we think it is necessary to do a brief description. We use the traditional classical PET image reconstruction algorithm to test the universality of all the sensors-ring systems. Firstly, we recombine the three-dimensional response lines data list into two-dimensional sine diagram by Fourier Rebining (FORE). On this basis, the Ordered Subset Expectation Maximization (OSEM) algorithm is used for imaging reconstruction. We use 3D-OSEM algorithm for imaging reconstruction, and the number of subsets is 13. The core iterative formula is shown in **Eq. (6)**.

$$\lambda_i^{k+1} = \frac{\lambda_i^k}{\sum_j a_{ij}} \sum_j \left[Y_j \frac{a_{ij}}{\sum_i a_{ij}\lambda_i^k} \right] \quad (6)$$

As shown in **Eq. (6)**, λ_i represents the grayscale value of the number i pixel in the image (in this article, it represents the event counts). a_{ij} represents the system matrix of the PET Full-Ring model. In this article, the angle information of the response lines data list in all Not-Full-Ring systems is converted into absolute angle, so the system matrix is calculated as the Full-Ring model ($D = 200mm$, 250mm and 300mm are different only in the space size of the system matrix). Y_j represents the number j response line, which is the number j element in the two-dimensional sine diagram. The image reconstruction process is completed in MATLAB, and the corresponding section slice imaging is generated according to the spatial coordinates of the required detection position.

According to the above experimental plan, the cross section of the nut on the lower part of the piston is imaged. As shown in **Figure 12.**, the slice imaging results of the 19 processes are presented. For the Sensing diameter $D = 250mm$ and 300mm,
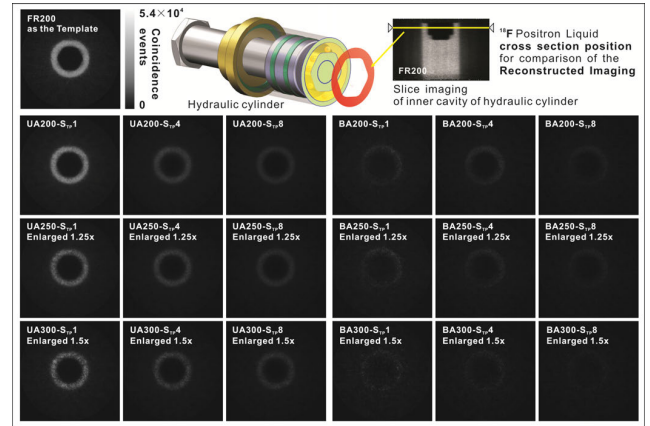

FIGURE 12. The slice imaging results of the 19 processes of the nut on the lower part of the piston. For the Sensing diameter D = 250mm and 300mm, the slice imaging has been simply enlarged and cut to 200mm in MATLAB.
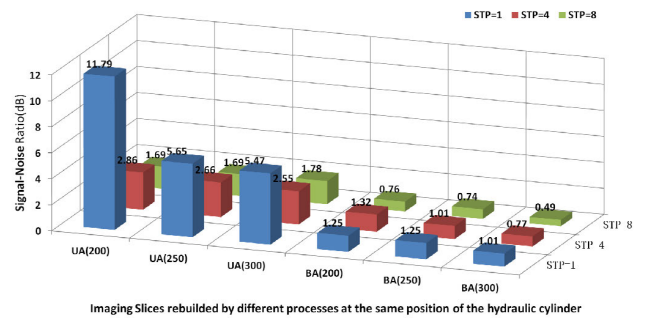

FIGURE 13. The SNR results of the 18 Not-Full-Ring processes. we use the classical Signal-Noise Ratio(SNR) method to evaluate the image quality of the 18 Not-Full-Ring processes, by using the FR(200) imaging as template.

the slice imaging has been simply enlarged and cut to 200mm in MATLAB.

In order to obtain objective and fair evaluation results, we use the classical Signal-Noise Ratio(SNR) method to evaluate the image quality of the 18 Not-Full-Ring processes, by using the FR(200) imaging as template. The SNR results are showed in **Figure 13**. The template image of FR(200) was used as signal, the image generated by each model subtracted the template image as noise. The calculation formula of SNR is shown in **Eq.(7)**. P_M refers to the images generated by each model, P_T refers to the template image gained by FR(200).

$$SNR = 10 * \log 10(\frac{P_M}{P_M - P_T}) \quad (7)$$

Firstly, the imaging quality of Uniform-arrangement and Bilateral-arrangement is compared. As shown in **Figure 13.**, The SNR values of all the Uniform-arrangement are higher than that of Bilateral-arrangement. In detail, using FR(200) image as template, all the Uniform-arrangements' SNR values are above 1. Especially when $S_{TP} = 1$, they are all higher than 5. However, the SNR values of Bilateral-arrangement was barely maintained around 1, some even less than 0.5. The

result of these SNR values are consistent with the conclusion of the previous simulation. As shown in **Figure 7. Photon energy distribution** of the previous section, the quantity of photons in Uniform-arrangement is larger than that in Bilateral-arrangement near 511kev$\pm$15%. This shows that Uniform-arrangement can collect coincidence events more sufficiently than Bilateral-arrangement.

Next, we analyze all the Uniform-arrangement and Bilateral-arrangement separately. In Uniform-arrangement, we can find that with the increase of sensing diameter D, the image quality decrease, but the D's influence on image quality is not as great as S_{TP}. As shown in **Figure 13.**, the integral multiple value of step angle has the key impact on imaging quality. The smaller the S_{TP} is, the higher the SNR values will be. We can also see from the **Figure 7. Photon energy distribution** that when $S_{TP} = 1$, no matter $D = 200$mm, 250mm or 300mm, the curve distributions are relatively close, but when $S_{TP} = 4$, the three curve distributions have a step decline. In Bilateral-arrangement, Since the SNR values of these styles in **Figure 13.** are very low, it is meaningless to discuss the influence of sensing diameter D and S_{TP} for this arrangement. So far, we have a good reason to believe that Uniform-arrangement has better sensing performance.

Finally, we compare the Uniform-arrangement style with the Full-Ring style. Because it is used to detect the liquid inside the metal cavity, it can be seen from **Figure 12.** that the liquid profile is not very clear even in the case of Full-Ring. The blocking of the metal cylinder wall does reduce the quantity of coincidence events received. But considering that we use the classical algorithm, there is no specific algorithm to deal with the scattering. In the experimental operation, we can also increase the amount of coincidence events by increasing the radioactivity in the liquid. There is much space for improvement in imaging quality. In Uniform-arrangement, when $D = 1$ and $S_{TP} = 1$, the SNR value is 11.79, It has been able to clearly reflect the characteristics as the template image done.

In summary, Not-Full-Ring sensors arrangement scheme for PET imaging is feasible. Sufficient source radioactivity, proper sensor arrangement, proper step angle and optimized imaging algorithm can make the imaging quality better.

V. CONCLUSION
Through this study, we believe that Not-Full-Ring system is feasible and effective to reduce the number of sensors and increase the flexibility of automation. This scheme is not only suitable for the research described in this article, but also suitable for other research projects that need to use PET imaging.

The unit-price of PET sensor is expensive. The essence of Not-Full-Ring sensors arrangement is to subdivide the demand of the research. In the case of meeting the core research objectives, some compromise or enhancement should be made in the aspects of sensitivity, R & D cost and versatility.

It is hoped that this article can provide an effective research method for the research team with similar technical needs.

REFERENCES
[1] C. Orlando, "Nose landing gear simple adaptive shimmy suppression system," *J. Guid., Control, Dyn.*, vol. 43, no. 7, pp. 1298–1312, Jul. 2020.

[2] M. Rahmani and K. Behdinan, "Structural design and optimization of a novel shimmy damper for nose landing gears," *Struct. Multidiplinary Optim.*, vol. 62, no. 5, pp. 2783–2803, 2020.

[3] D. Cristiani, L. Colombo, W. Zielinski, C. Sbarufatti, F. Cadini, M. Dziendzikowski, and M. Giglio, "On the evaluation of a coupled sequential approach for rotorcraft landing simulation," *Sensors*, vol. 20, no. 9, p. 2540, Apr. 2020.

[4] R. M.-M. Merino-Martinez and G. areth, "Multi-approach study of nose landing gear noise," *J. Aircraft*, vol. 57, no. 3, pp. 517–533, 2020.

[5] J. Józwik, J. Michaáowska, A. Tofil, D. Báejczak, and J. Laskowski, "Determining wheel forces and moments on aircraft landing gear with a dynamometer sensor," *Sensors*, vol. 20, no. 1, p. 227, Dec. 2019.

[6] X. Yang, "Multiple-particle tracking-an improvement for positron particle tracking," *Nucl. Inst. Methods Phys. Res. A*, vol. 564, no. 1, pp. 332–338, 2006.

[7] D. J. Parker and X. Fan, "Positron emission particle tracking—Application and labelling techniques," *Particuology*, vol. 6, no. 1, pp. 16–23, Feb. 2008.

[8] S. Beer, "Design and initial performance of PlanTIS: A high-resolution positron emission tomograph for plants," *Phys. Med. Biol.*, vol. 55, no. 3, p. 635, 2010.

[9] Q. Wang, "A dedicated high resolution PET imager for plant sciences," *Phys. Med. Biol.*, vol. 59, no. 19, pp. 5613–5629, 2014.

[10] H. Tashima, Y. Hirano, S. Kinouchi, E. Yoshida, H. Ito, and T. Yamaya, "Theoretical and numerical analysis of the single-ring OpenPET geometry for in-beam PET," in *Proc. IEEE Nucl. Sci. Symp. Med. Imag. Conf. Rec. (NSS/MIC)*, Oct. 2012, pp. 1–5.

[11] R. R. Raylman, A. V. Stolin, P. F. Martone, and M. F. Smith, "TandemPET–A high resolution, small animal, virtual pinhole-based PET scanner: Initial design study," *IEEE Trans. Nucl. Sci.*, vol. 63, no. 1, pp. 75–83, Feb. 2016.

[12] Correcher, C., Molinos, "Cesar, Vidal, a PET design based on SiPM and monolithic LYSO crystals: Performance evaluation," *IEEE Trans. Nucl. Sci.*, vol. 63, no. 5, pp. 2471–2477, Dec. 2016.

[13] Y. Chen, K. Saha, and S. J. Glick, "Investigating performance of limited angle dedicated breast TOF PET," in *Proc. IEEE Nucl. Sci. Symp. Conf. Rec.*, Valencia, Spain, Dec. 2011, pp. 2346–2349.

[14] T. Kobayashi and K. Kitamura, "Design considerations for a partial-ring, multi-modal compatible whole-body TOF PET scanner: Flexible PET," in *Proc. IEEE Nucl. Sci. Symp. Med. Imag. Conf. Rec. (NSS/MIC)*, Oct. 2012, pp. 2807–2812.

[15] C. Liu, "Design and evaluation of gapless curved scintillator arrays for simultaneous high-resolution and high-sensitivity brain PET," *Phys. Med. Biol.*, vol. 64, no. 23, 2019, Art. no. 225014.

[16] H. Xiao, M. Zhao, J. Liu, and H. Chen, "A study on scattering correction for μ-photon 3D imaging test method," *AIP Adv.*, vol. 8, no. 3, Mar. 2018, Art. no. 035315.

[17] H. Xiao, M. Zhao, J. Liu, J. Liu, and H. Chen, "A new method for spatial structure detection of complex inner cavities based on 3D μ-photon imaging," *AIP Adv.*, vol. 8, no. 5, May 2018, Art. no. 055205.

CHEN HAO was born in Shaoxing, Zhejiang, China, in 1986. He received B.Eng. degree from the Nanjing University of Aeronautics and Astronautics, China, in 2013, where he is currently pursing the Ph.D. degree with the College of Automation Engineering. His research interests include positron nondestructive testing, algorithm optimization, and image processing.

RUIPENG GUO received the Ph.D. degree in instrument science and technology from Shanghai Jiaotong University, Shanghai, China, in 2011. She is currently an Associate Professor with the Nanjing University of Aeronautics and Astronautics. Her research interests include non-destructive testing, computer measurement, and control and signal processing.

MIN ZHAO was born in Nanjing, Jiangsu, China, in 1959. He received the Ph.D. degree from the College of Automation Engineering, Nanjing University of Aeronautics and Astronautics, China. He is currently a Professor with the Nanjing University of Aeronautics and Astronautics. His research interests include positron nondestructive testing, sensors, and signal processing.

MINGWEI ZHU received the master's degree in measurement technology and instruments from the Kunming University of Science and Technology. She is currently pursing the Ph.D. degree with the College of Automation Engineering, Nanjing University of Aeronautics and Astronautics. Her research interests include deep learning and image processing.

MIN YAO received the B.Sc., M.Sc., and Ph.D. degrees from the Nanjing University of Aeronautics and Astronautics, China, in 1997, 2002, and 2008, respectively. She is currently an Associate Professor with the Nanjing University of Aeronautics and Astronautics. Her research interests include computer measurement, control and UAVs task assignment, data and signal processing, and algorithm optimization.

XIAO HUI received the Ph.D. degree with the College of Automation Engineering, Nanjing University of Aeronautics and Astronautics (NUAA), Nanjing, China, in 2020. He is currently a Post-Doctoral Researcher with the College of Computer Science and Technology, NUAA, and the Shenzhen Research Institute, NUAA. His main research interests are photon imaging testing technology and 3-D image reconstruction algorithms based on AI.

. . .